PURGE-MAINSTREAM INTERACTIONS IN A TURBINE STAGE WITH ROTOR ENDWALL CONTOURING

Alex W. Mesny[1] **Oliver J. Pountney[1]** **James A. Scobie[1]**

Yan Sheng Li[2] **Carl M. Sangan[1]**

[1]Department of Mechanical Engineering, University of Bath, Bath, United Kingdom.

[2]Siemens Industrial Turbomachinery Ltd., Lincoln, United Kingdom.

**Corresponding Author's Email: c.m.sangan@bath.ac.uk*

ABSTRACT

Purge flows are prevalent in modern gas turbine design allowing for increased turbine entry temperatures. The purge flow passes through a rim seal and interacts with the mainstream flow, modifying the blade secondary flow structures and reducing stage efficiency. These structures may be controlled using End Wall Contouring (EWC), though experimental demonstration of their benefit is seldom reported in the literature. The optically accessible turbine at the University of Bath was designed to directly measure and visualize the flow field within the blade passage for a rotor with EWC.

The single-stage turbine enables phase-locked flow field measurements with volumetric Particle Image Velocimetry (PIV). Purge flow was supplied to investigate a range of operating conditions in which the secondary flow structures were modified. The modular turbine rotor allowed for expedient change of a bladed ring, or bling, featuring non-axisymmetric EWC.

The identified secondary flow structures were the Pressure-Side leg of the Horse Shoe Vortex (PS-HSV) and an Egress Vortex (EV) of concurrent rotational direction. An increase in purge flow rate monotonically shifted the EV toward the suction-side (SS) of the adjacent blade. The migration of the PS-HSV towards the SS caused the two aforementioned vortices to merge.

The EWC rotor design included a Leading-Edge (LE) feature to alter the PS-HSV, and a trough to guide the EV low spanwise in the passage and maintain displacement from the adjacent suction side. The EWC rotor was found to be effective at altering the formation and positioning of the secondary flow structures at a range of purge flow conditions.

Keywords: Axial Turbine, Secondary Flows, Purge, Volumetric Velocimetry, Endwall Contouring

1. INTRODUCTION

Secondary flows are fluid dynamic structures that have components of velocity differing from the bulk flow direction. In the context of gas turbine engines, secondary flows introduce blade row loss mechanisms that significantly reduce turbine stage efficiency [1]. Classical blade passage secondary flows consist of the Horse Shoe Vortex (HSV), corner vortices, tip leakage vortices and the Passage

Vortex (PV) [2]. The PV is a broad term that is used to denote the dominant vortex in the passage; the Pressure-Side leg of the HSV (PS-HSV) merges into the PV as it migrates across the passage due to the transverse pressure gradient.

The classical description of secondary flows outlined above does not consider the effects of the purge flow. Purge flow is introduced to the wheelspace cavity between the rotor and stator to limit or prevent ingress of hot mainstream gas from the turbine annulus into the wheelspace. The purge flow exits the wheelspace through the rim seal into the mainstream gas path, forming an Egress Vortex (EV) [3]. It is worth noting that an EV will form even when there is zero purge supply to the wheelspace – this is the result of continuity of mass when ingress occurs. The EV and PS-HSV merge in the downstream blade passage, forming a strengthened PV. These secondary flow structures spoil blade aerodynamics, including the generation of entropy within the stage and localized modification of flow angles, ultimately reducing efficiency.

Shaping the turbine endwall to increase efficiency is not a recent development (e.g. [4]-[6]). Fillet radii between blades and the hub have been utilized for many generations of turbines, to reduce the strength of corner vortices. More complex shaping of the rotor hub requires numerical optimization schemes that aim to increase efficiency or reduce secondary kinetic energy (SKE), for example. Typical non-axisymmetric End Wall Contouring (EWC) include Leading-Edge (LE) features to alter the formation of the HSV, or curvature on the rotor hub to modify the pressure field and control the passage vortex, as shown in Fig. 1.

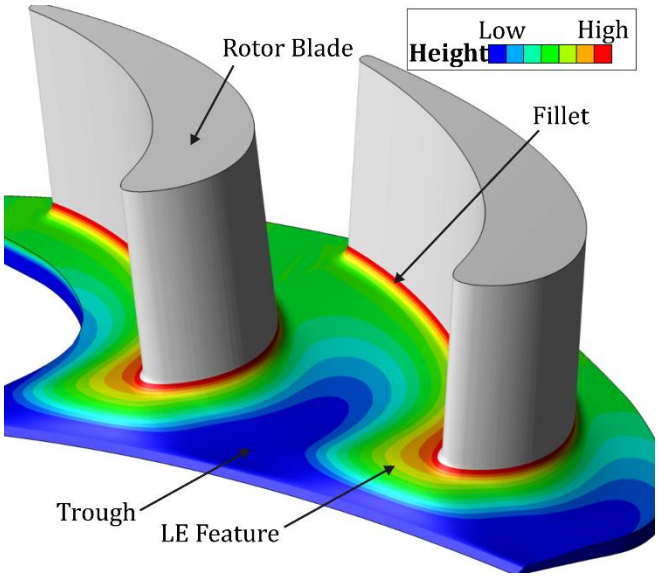

FIGURE 1: ENDWALL CONTOURING ON A TURBINE BLADE ROW. ARBITRARY CONTOUR SHOWS POSITIVE AND NEGATIVE ENDWALL DISPLACEMENT.

Non-axisymmetric EWC has been proposed and implemented with mixed success in recent years. EWC frequently underperforms when employed in experimental or operational turbines, relative to numerical simulations (e.g. [7] - [9]). The engine designer must

successfully use EWC to increase efficiency whilst ensuring that rim-seal performance or mechanical integrity of the components is not compromised. A combined design of rim seal geometry and mainstream EWC is required for this purpose.

An optically accessible turbine at the University of Bath was specifically designed to measure and visualize the flow field within a turbine with non-axisymmetric EWC [10]. Volumetric particle image velocimetry (PIV), also known as volumetric velocimetry (VV), was applied to the experimental turbine, both with and without EWC.

Section 2 of this paper reviews relevant literature in turbine secondary flows and the generation and application of EWC to turbine rotors. Section 3 contains the experimental methodology of this study, from the mechanical and optical design of the test turbine to the data processing required to understand the VV measurements. Section 4 contains the results and discussion of a range of flow conditions on two rotor designs, showing how EWC modified the secondary flow structures.

2. LITERATURE REVIEW

The literature review is presented in two parts: Section 2.1 provides an overview of secondary flow studies in turbines with egress and Section 2.2 briefly reviews recent EWC research, with a focus on those with experimental validations of non-axisymmetric EWC and purge flows.

2.1 Secondary Flows in Turbines

Classical secondary flow structures were described by Langston [2]. The subsequent advancement of both numerical simulations and experimental measurement techniques has since enhanced predictions of the formation, displacement and strength of the secondary flow field.

Unsteady Reynolds-Averaged Navier-Stokes (URANS) Computational Fluid Dynamics (CFD) was utilized by Schneider *et al.* [11] to predict the formation of secondary flow structures within the rotor passage. While the Nozzle Guide Vane (NGV) flow field conformed to classical flow roll-up, the downstream rotor HSV was found to be associated with shed vortical structures from the NGVs. The authors highlight the requirement for turbine simulations and experiments featuring rotation to capture these complex interactions.

The introduction of purge flow to a turbine stage has been found to fundamentally change the secondary flow structure and stage performance. Schuepbach *et al.* [12] measured an efficiency loss of 0.6% with the inclusion of 0.9% purge flow. This was associated with radial migration of the secondary structures measured downstream of the stage. Notably, peak vorticity was reduced with purge, but the overall circulation was increased. The same facility was used by Regina *et al.* [13] to quantify the efficiency loss over a range of purge-mainstream mass fractions (*MF*). Time-resolved data revealed that the interaction between the purge and the mainstream was periodic, leading to a change in both the strength and position of the measured secondary flow features at a given instance.

Schrewe *et al.* [14] used temperature measurements to track the entrainment of purge flow into the secondary flow structures in a large-scale turbine rig. The authors note four main sources of loss due to the use of purge flow, including the egress acting as a blockage in the blade passage and an intensification of the secondary flow structures. This blockage led to movement of the egress plume towards the SS with increased purge flow rates.

The three-dimensional flow field within a rotating turbine blade passage was experimentally measured by Mesny *et al.* [3] with and without purge. The use of VV revealed the migration of the PS-HSV across the passage to merge with the EV, forming a single vortex structure denoted as the PV. As the purge flow rate was increased, the EV emerged closer to the SS and delayed the merging of the two vortices. Circulation, analogous to vortex strength, was enhanced with purge.

Recently, Barsi *et al.* [15] used URANS CFD to investigate the impact of purge-mainstream interaction on losses in the annular region between the vane trailing edge and rotor leading edge. The authors' computations showed that in this region losses were double for the case where purge flow was modelled relative to the case without. Although losses within the downstream blade passage were not computed, the authors noted that the purge-mainstream interaction modified the angle of the flow at the blade leading edge, producing a 'detrimental carryover effect'.

Coull & Clark [16] used RANS CFD to investigate the effect of inlet flow conditions on the endwall losses in a turbine cascade. Although purge flow was not modeled, the endwall losses estimates showed a high degree of sensitivity to conditions at the inlet, varying by a factor of three for the scenarios modeled in the paper. The authors cite several strategies to reduce endwall losses, with two particularly pertinent to this paper: first, the need for careful design of the rim seal geometry to help condition the inlet flow; and second, the use of EWC to control the path of vortical secondary flow structures, with aim of minimizing associated SKE.

2.2 Endwall Contouring

While numerous studies exist before the publication of Rose's 1994 paper [4], advances in CFD allowed for the author to optimize the design of non-axisymmetric NGV EWC. The target function was to reduce pressure non-uniformities that drive ingress and therefore limit the purge required to seal the wheel-space. Rose concludes with caution that NGV EWC may modify aerofoil flow distributions, thereby removing any benefits that the new design may have had.

Target functions, therefore, play a critical role in the apparent success of an EWC design. Bergh *et al*. [7,8] present a two-part study on EWC optimization using a range of objective functions on the same 1.5-stage experimental turbine. The eight functions of variable complexity generated a significant variety of EWC shapes; from the classical PS peak and SS trough to intricate multi-lobed designs. These studies, including a follow-up paper [9], are examples of the trend of numerical predictions to inconsistently align with

experimental results in the field of EWC optimization. Of the four experimentally tested EWCs, one had an underpredicted efficiency gain, another an overpredicted efficiency gain and two demonstrated efficiency losses, relative to the baseline rotor. These results are useful to engine designers in displaying the sensitivity of predictions to the target function; however, understanding the causes for the differences between the predictions and the experiments is necessary.

The optimization of Bergh *et al*. does not use purge flow, which may explain the numerical and experimental discrepancies. Other studies, such as Chilla *et al.* [17], include the rim seal and cavity in the numerical domain. The authors sought to increase efficiency and reduce ingestion with a non-axisymmetric feature on the rim seal. The final design was predicted to be successful, and it was recommended that the level of purge flow could be reduced to further benefit efficiency, however, no experimental validation of this design was provided.

The LISA turbine at ETH Zurich has featured in several EWC studies [18-20]. While the experiments were conducted on engine realistic architecture that included egress, the supporting CFD was performed without this key feature. The efficiency was increased but the interaction between the purge and secondary flows was highlighted. The turbine efficiency was more sensitive to purge in the presence of EWC compared to the baseline cylindrical rotor: an increase from -0.6% to -0.87% efficiency per 1% purge.

Industry-based research from Hu & Luo [21] offers useful insight into the inclusion of purge flow in EWC design. In a numerical study, the EWCs are separately designed with and without purge flow with the objective of reduced total pressure loss. The EWC without purge gave a 10% reduction in total pressure loss. However, when purge flow was introduced, the improvement was reduced to just 1.36%. In contrast, the EWC that was optimized with purge produced a 9.8% reduction in total pressure losses compared to the baseline at the operational point. The EV strength was reduced by the relevant EWC, and the authors suggest that contouring should extend upstream of the LE to the rim seal for improved control of the egress flow.

Recent research by Schäflein *et al.* [22] showed a similar result. The predicted performance of the optimized EWC was high, however the inclusion of purge flow eliminated any benefit that the new design indicated. The efficiency of the stage was reduced with the EWC due to the enhancement of the secondary flow structures with purge.

There exists a disconnect between the predicted and experimentally determined performances of rotors with EWC. Interrogation of the fluid dynamics within the blade passage will allow the interaction between the mainstream gas path, purge flow and EWC to be better understood.

3. METHODOLOGY

This section describes the mechanical and optical design of the experimental test turbine at the University of Bath. Data processing of the three-dimensional flow field is also discussed. The maturity of this experimental setup is outlined by previously published papers with similar methodologies [3,10].

3.1 Mechanical Design

The University of Bath optically accessible single-stage turbine (Fig. 2) was specifically designed to investigate the effect of endwall contouring on the secondary flow field in the rotor blade passage. This task dictated a number of design challenges to be overcome; stable aerodynamic operation, particle seeding, optical access for illumination and image capture, importantly alongside expedient rotor bladed-ring (bling) changes.

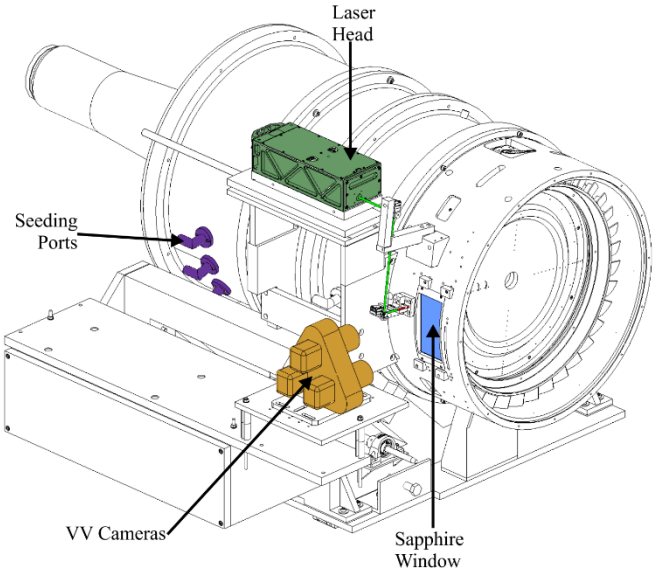

FIGURE 2: UNIVERSITY OF BATH OPTICALLY ACCESSIBLE TURBINE [7].

The mainstream gas path was supplied by a screw compressor to maintain a constant flow coefficient. The air, delivered via a 6" inlet pipe, up to 1.2 *barg* and a constant mass flow rate of 1.105 ± 0.005 kg/s to give $Re_x = 2.2 \times 10^5$. From the inlet pipe, the air enters the rig into a settling chamber containing baffles to promote mixing with seeding particles, and a turbulence grid to maintain the radially invariant turbulence intensity, σ, of 5%, measured between the boundary layer and the annular midspan.

The blading of this experimental facility was based on a Siemens Energy turbine. The stage consisted of 24 vanes and 36 prismatic, low-aspect ratio blades with a design promotes secondary flow formation. The power generated by the blades was absorbed by a dynamometer to maintain a constant rotational speed of 900 RPM, to give $Re_\Phi = 5.9 \times 10^5$. Whilst this is an order of magnitude lower than an operational gas turbine, the flow coefficient of 0.38 is representative.

The flow field within the rotor blade passage was interrogated using a three-dimensional particle image velocimetry technique known as VV. This method, as with other PIV, requires seeding particles to be distributed within the measurement fluid. 1 μm olive oil particles within the turbine have a Stokes number, St, of 0.012; with $St < 0.1$, seeding particles will follow streamlines in the flow to within 1%. Olive oil particles were supplied using droplet generators and the output particle density was related to the inlet pressure, which was independently controlled from the mainstream gas path pressure.

The Siemens Energy turbine stage contains a purge flow, hence it was necessary to simulate this within the experimental turbine. Purge was supplied using a compressed air source, controlled separately from the mainstream gas path allowed for a range of mainstream to purge flow mass fractions, MF. The purge flow was supplied at low radius to the rotor-stator cavity prior to ejection into the gas path via a double radially-overlapping chute seal at the periphery of the wheel-space.

The rotor was of modular design, and expedient change of geometry was achieved via blings. The second of the two rotor blings featured non-axisymmetric EWC. The EWC was designed via a feature-based approach, as opposed to an optimizer coupled with an objective function. The philosophy of the feature-based approach was to control the purge flow interaction with the mainstream gas path through parameterized geometric features in the passage: a suction-side trough, a pressure-side trough and a blade leading-edge feature. The design of this EWC was the subject of Schreiner *et al.* [23] and corresponds to EWC-008 in that study, with the assessment of EWC designs in Fig. 3. The EWC features a trough near to the suction surface and a leading-edge feature at the PS LE. Both rotors feature 3.5 mm fillet radii at the blade root and span the 40 mm annulus with a tip clearance of 0.5 mm.

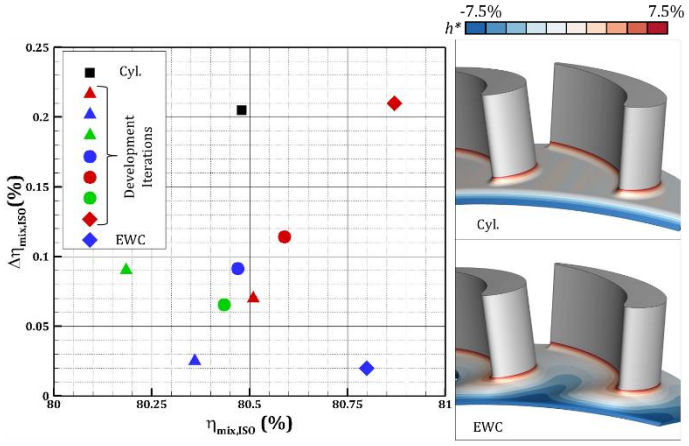

FIGURE 3: UNSTEADY FLUCTUATION IN STAGE EFFICIENCY AGAINST MAGNITUDE OF STAGE EFFICIENCY FOR THE CYLINDRICAL AND EWC ROTORS, FROM [23]. INSETS OF BLADE SECTORS COLORED BY SURFACE HEIGHT AS A PERCENTAGE OF SPAN, $h*$.

From Fig. 3, the selection of the EWC for further study was apparent through minimal unsteady fluctuations in efficiency within a blade pass, as this is a measure of endwall flow that is not separated. Whilst overall stage efficiency was predicted to be higher in a previous development of the EWC, that design featured high fluctuations, and would likely have shown poor performance in the experimental turbine.

The operating conditions of the experimental facility are given in Table 1:

TABLE 1: OPERATING PARAMETERS OF THE TURBINE STAGE.

Parameter	*Value*
Disc speed (rpm)	900
Rotational Reynolds Number, Re_ϕ	5.9×10^5
Axial Reynolds Number, Re_x	2.2×10^5
Flow Coefficient, C_F	0.38
Vane exit Mach Number, M	0.12
Degree of Reaction, Λ	0.21
Blade Loading Coefficient, Ψ	2.2
Blade Aspect Ratio (= b/c_{ax})	0.73
Blade Turning Angle (°)	104
Purge-Mainstream Mass Fraction, MF	0% - 1.7%

3.2 Optical Design

Optical access was one of the key design requirements for this turbine stage. The three-dimensional particle image velocimetry (VV) technique required camera access for a triplet of 8 MP charge-coupled device (CCD) cameras fitted with 75 mm lenses, and laser access for a 200 mJ Q-switched 532 nm laser cone.

The cameras were mounted in an anti-vibrational mount on a breadboard table for precise positioning relative to the stage. A window was located in the rotor casing for camera access with the cameras pointed at the rotor endwall. The sapphire window is plano-concave, where the inner radius was matched to the rotor casing (352 mm) to minimize aerodynamic interactions.

This curvature has the side-effect of acting as a lens, hence VV calibration occurred with the window in situ. VV calibration consisted of traversing an illuminated dot plate through the measurement volume. Cameras were focused on specific regions within the blade passage to ensure high-quality data, and hence multiple calibrations were required to complete each interrogation volume. A static calibration using a fixed plate with a fiducial point of known position relative to the turbine axis was used to transform data from all calibrations onto the same absolute reference frame.

Laser access for particle illumination was achieved using a custom optic pathway, designed for minimum interaction between the optical and gas pathways. The first component in the optical pathway was a variable focus, positive focal length lens. This allowed for

a reduction of the beam diameter, though care was taken in ensuring that the beam was not focused in free space, as this can cause ionization of air for this high laser power.

The optical pathway consisted of fused silica prisms on kinematic mounts for precision control of the laser into the custom borescope. The borescope was a 5 mm inner diameter tube with a plano-concave lens and prism mounted at the far end. The 6 mm fused silica lens was mounted with negative focal length, hence the beam expanded into a cone as it was turned ninety degrees by the fused silica (or sapphire) substrate prism, as shown in Fig. 4.

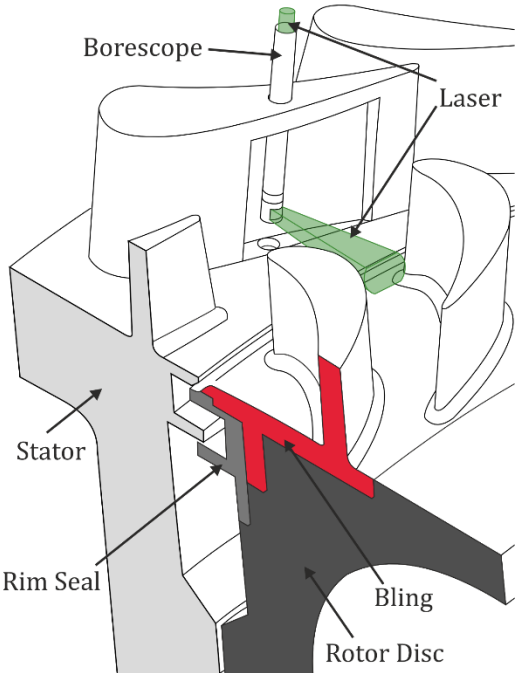

FIGURE 4: TURBINE CROSS SECTION WITH LASER DELIVERY; MODULAR ROTOR BLING HIGHLIGHTED.

The borescope was situated within a hollow, additively manufactured vane. An NBK-7 window sealed the optic vane; the outer surface was matched to the curvature of the SS to within 50 µm. The borescope was manually rotated about and traversed along its axis. This was necessary as the laser core cannot illuminate the entire passage with superposition of datasets required to complete a blade passage.

Synchronization of the data capture to the rotor was achieved using an optical sensor mounted on the back of the rotor disc. A signal was sent once per revolution to a TSI Synchronizer, whilst the timing settings were computer controlled. Delays were built into the triggering system to ensure that the blade passage was in full view of the cameras at data capture, with a $\Delta t = 10$ µs interval between laser pulses. The trigger delay led to a fixed rotor-stator clock angle chosen to fully occupy the field of view.

3.3 Data Processing

Data were captured by a workstation with dual six-core (12 thread) CPUs and 128GB RAM, required for expedient processing and temporary image storage respectively. The software used for these processes was TSI V3V Insight 4G (ver.4).

Following the trigger from the rotor sensor, the three camera sensors were exposed and a pulse of laser light occurred. After Δt = 10 μs, a second set of three images were captured, hence six images were captured per blade pass. Vector yield on any given six images is low, so each set of data consists of 200 image sextets at the same laser position.

Once collected, the data were pre-processed using minimum intensity subtraction, to reduce background reflections, and both gaussian and median filters to enhance particle identification. Particle identification, matching and tracking occurred using TSI's DPIR algorithm [24]. In the previous study by this group [3], the final data output was gridded; the 200 sextets of instantaneous velocities were interpolated onto a 1 mm grid. This study differs by post-processing the 200 unstructured datasets for each laser position together with a final interpolation for plotting purposes only. This unstructured processing was necessary to enhance data fidelity and reduce noise, which had hindered vortex tracking quality.

Within the MATLAB post-processing algorithm, the data were first transformed onto the absolute reference frame and then a series of spatial and statistical filters were applied. Spatial filtering removed low-quality data outside of the intended field of view and also removed the large number of spurious vectors associated with reflections from the hub and blade surfaces.

Statistical filtering was achieved using a Median Average Deviation (MAD) filter, as this was effective in removing outliers in data with large magnitudes in velocity components. The unstructured dataset contained noisy data of similar magnitude with different directions to the bulk flow, hence a vector difference test was applied. This algorithm was adapted from [25] for the unstructured 3D data from the original algorithm designed for gridded 2D PIV data.

$$\left|\vec{V}_{diff}\right| = \left|\vec{V}_{3D}(N) - \vec{V}_P\right| < \varepsilon_{thresh} \qquad (1)$$

A k-dimensional tree range search on every vector was used to locate every neighbor vector, $\vec{V}_{3D}(N)$, in a 1 mm search radius from every other vector in the field. For a vector to pass the filter, it must have at least 40 neighbors and for at least half of them to have a difference magnitude of less than 10 m/s, ε_{thresh} . That is, the query vector, $\vec{V}_P$, is subtracted from a neighbor and the magnitude of the difference, $\left|\vec{V}_{diff}\right|$, is used as a filter criterion. Algorithm settings were iterated until the final vector fields appeared with minimal noise, but care was taken to ensure the final field was not sparse.

A vortex tracking parameter, derived by Graftieaux *et al.* [26] was applied to the velocity field. The parameter, γ_2, indicates regions where vortical structures are located, with a theoretical boundary of $\gamma_2 = 2/\pi$. This parameter does not rely on velocity derivatives and was developed for use in relatively noisy PIV data. A centroid approach developed in the previous study [3] was used to track the vortex cores throughout the blade passage.

$$\gamma_2(P) = \frac{1}{N}\sum_{A}\frac{\left[\overrightarrow{PM} \times \left(\overrightarrow{V_M} - \overrightarrow{\tilde{V}_P}\right)\right].\vec{n}}{\left\|\overrightarrow{PM}\right\|.\left\|\overrightarrow{V_M} - \overrightarrow{\tilde{V}_P}\right\|} \quad (2)$$

$$\overrightarrow{\tilde{V}_P} = \frac{1}{N}\sum_{A}\overrightarrow{V_M} \quad (3)$$

Where *P* is the query point, *N* is the number of neighbor vectors *M* within area, *A*. *PM* is the positional vector between the query point and the neighbor vector and *n* is the normal to the plane.

Further post-processing required the use of Tecplot 360 EX for velocity derivate-based approaches, including *Q*-criterion [27], non-dimensional vorticity, ω^* and circulation. Tecplot afforded more performance for the densely populated unstructured datasets and was used to smooth the fields for comparison with the Graftieaux γ_2 parameter.

$$Q = \frac{1}{2}[\|\Omega\|^2 - \|S\|^2] \quad (4)$$

$$\omega^* = \left[|\omega|\frac{c_{ax}}{u_{in}}\right].[sgn(\omega_x)] \quad (5)$$

Where Ω and *S* are the anti-symmetric and symmetric components of the velocity gradient tensor – as referred to in [27] - respectively, $|\omega|$ is the magnitude of the vorticity, c_{ax} is the axial chord length (≈ 54 mm), u_{in} is the average axial component of velocity at the inlet plane (≈ 12.7 m/s), and $sgn(\omega_x)$ is the sign of the *x*-component of vorticity.

4. PURGE-MAINSTREAM INTERACTIONS

This section contains three-dimensional flow-field analysis of the rotor blade passage. A range of *MF* conditions are first analyzed for the cylindrical rotor. This is to establish and characterize the baseline secondary flow field behavior. In the following subsection, the data are compared to that of the rotor with EWC to isolate the effect of the contour design on the secondary flow field.

4.1 Baseline Rotor Flow Field

The measurement volume existed within a single turbine blade passage and occupied a region of up to 80% of the blade pitch, 60% of the axial chord, and 40% of the blade span. There are areas within the measurement volume with limited quality of data, due to reflections and laser access; the volumetric extent of the datasets were variable. The measurement volume was partitioned with slices at arbitrary axial positions for ease of data visualization.

Axial slices at x/c_{ax} = 10%, 20% and 30% are shown with in-plane velocity streamlines and a contour of normalized velocity magnitude (Fig. 5). Each row represents an increasing purge-mainstream mass-fraction from 0% to 1.7%. The in-plane velocities have been annotated with vortex core positions obtained from the γ_2 centroid method outlined in Section 3.3. As identified by Mesny *et al.* [3], the left of the two vortex cores is the EV and the right is the PS-HSV. For the 0% MF case, the EV was formed entirely from ingested fluid. At 0.26% and 0.52% MFs, the EV constitutes a mixture of ingested fluid and superposed purge flow; when fully sealed at the two higher MFs [10] – i.e. in the absence of ingress - the EV constitutes solely purge flow.

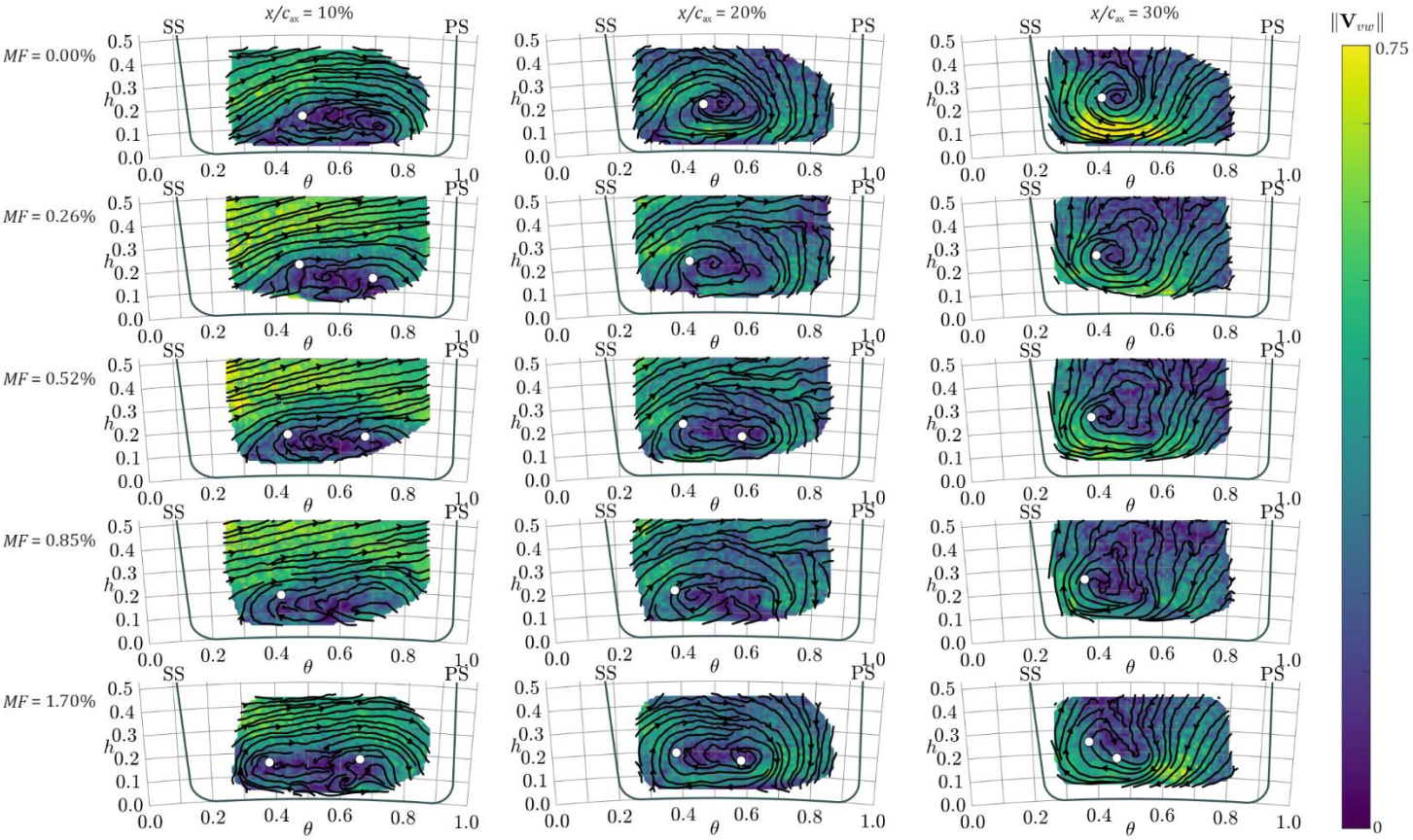

FIGURE 5: IN-PLANE VELOCITY STREAMLINES AT AXIAL PLANES x/c_{ax} = 10%, 20% AND 30%, CONTOUR OF NORMALIZED IN-PLANE VELOCITY MAGNITUDE. EACH ROW REPRESENTS A PURGE-MAINSTREAM *MF* FROM 0.0% TO 1.7%. WHITE CIRCLES REPRESENT VORTEX CORES.

In any given column, the effect of the purge flow is shown in both the distribution of the velocity and the location of the vortex cores. Consider the first column, which represents the early passage at x/c_{ax} = 10%: the presence of two vortical structures is observed for all MFs, though the increase in purge tends to show the displacement of one of the cores towards the adjacent SS. The emergence of the EV core shifts towards the SS by 10% of the blade pitch from 0% to 1.7% MF. Deeper into the passage, the two-vortex system is reduced to a single vortex, where the increase in purge correlates to a delayed merging. The intermediate flow rates, not previously published, follow the trend of the extrema in *MF*.

The core locations were computed throughout the measurement volume and are plotted in cascade view in Fig.6. The radial extent of the vortex cores does not significantly vary between the *MF*s, hence the meridional view has been omitted. In all cases, the PS-HSV emerges in close proximity to the PS LE. It should be noted that due to the adjacent blade fillet, the volumetric PIV data quality is affected and hence between data sets there is some difficulty in tracking the PS-HSV. Despite this, it is apparent that the increase in purge flow does not directly affect the formation of the PS-HSV.

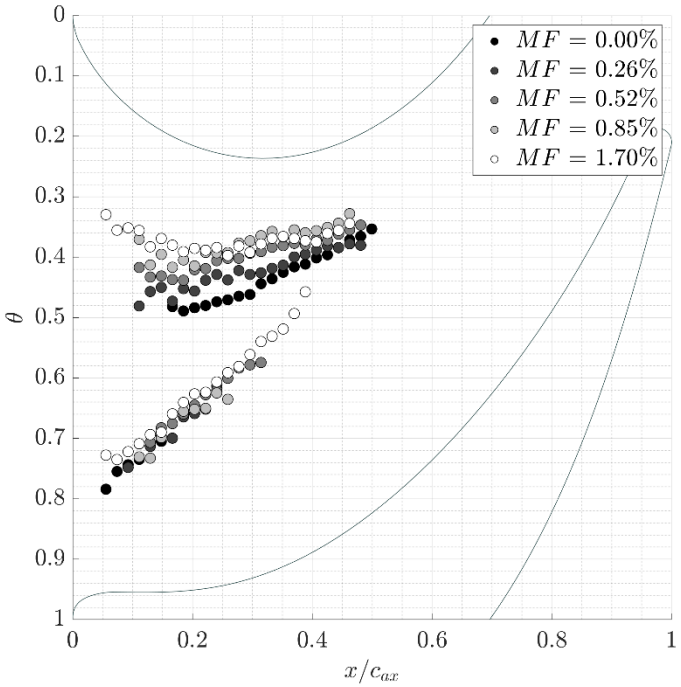

FIGURE 6: CASCADE VIEW OF VORTEX CORES AT A RANGE OF *MF* FOR THE CYLINDRICAL ENDWALL ROTOR.

Conversely, the EV is affected by the increase in purge flow rate. In the 0% *MF* case, the EV is initially located at $\theta \sim 0.5$. Subsequently, a monotonic shift of the EV towards the SS is seen with purge flow. At the lower MFs (0-0.52%), ingress into the rotor-stator cavity is expected as the purge flow is insufficient to reach a fully sealed rim-seal condition [10]. However, there is not a significant change in behavior of the secondary flow structures when purge flow is increased to fully seal the cavity; the monotonic trend continues.

The displacement of the egress core towards the SS correlates to the reduction in stage efficiency that is widely reported in the literature. The close proximity of the secondary flow structure to the blade causes aerodynamic spoiling, reducing the power produced. This highlights the need for EWC to help control the location and formation of the secondary flow structures.

4.2 Flow Field with Rotor Endwall Contouring

Volumetric velocimetry measurements were obtained for the EWC rotor. The blade passage velocity field was used to assess whether the EWC successfully alters the secondary flow structures in pursuit of improved stage efficiency.

As with Fig. 5, in-plane, two-dimensional velocities at axial slices throughout the measurement volume are a useful tool for assessing the secondary flow field of the EWC rotor. Fig. 7 has been annotated with both the vortex cores of the EWC secondary flow field (diamonds), but also the vortex cores of the equivalent flow condition case from the baseline rotor (circles). To aide visual clarity, three of the EWC datasets are displayed in Fig. 7. The shape of the EWC has been superimposed on the plot as a red line at the hub.

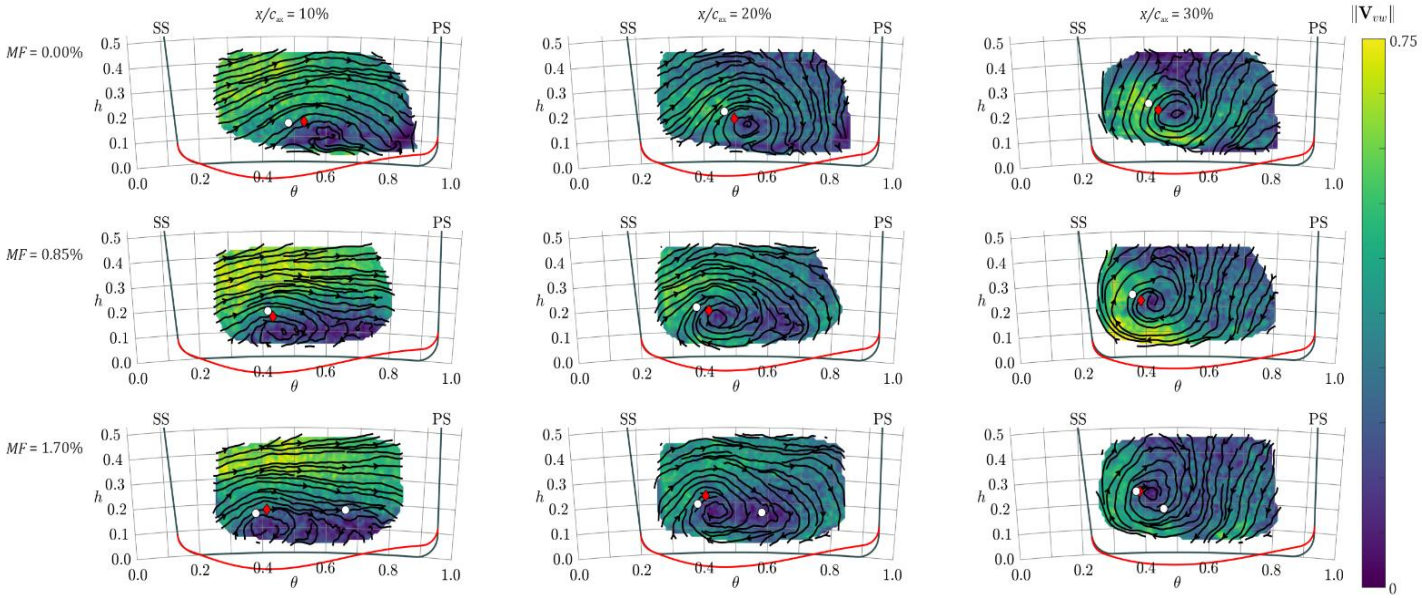

FIGURE 7: IN-PLANE VELOCITY STREAMLINES AT AXIAL PLANES x/c_{ax} = 10%, 20% AND 30% FOR THE EWC ROTOR, CONTOUR OF NORMALIZED IN-PLANE VELOCITY MAGNITUDE. EACH ROW REPRESENTS A PURGE-MAINSTREAM *MF* FROM 0.0% TO 1.7%. WHITE CIRCLES REPRESENT CYLINDRICAL ROTOR VORTEX CORES; RED DIAMONDS FOR THE EWC. RED LINE IS EWC AT EACH AXIAL LOCATION.

The analysis shall primarily focus on the EV/PV as these are the predominant secondary flow features in the blade passage; the PS-HSV is inconsistently tracked. The EWC design presents a two-fold challenge for data collection close to the PS. Firstly the LE feature causes the laser light to be reflected into the camera, obfuscating particles in that region. Secondly the feature was designed to reduce the strength of the PS-HSV, ergo making it difficult to capture experimentally.

Despite this, modification of the secondary flow features in the passage is apparent through comparison of the core locations. In general, the EWC rotor has an EV both radially lower and further away from the adjacent SS. The EV and the subsequent PV are circumferentially aligned to the trough feature of the EWC shown by the surface below $h = 0$. The EWC affects the positioning of the secondary flow structures. To emphasize this, a cascade view of the vortex cores is presented in Fig. 8.

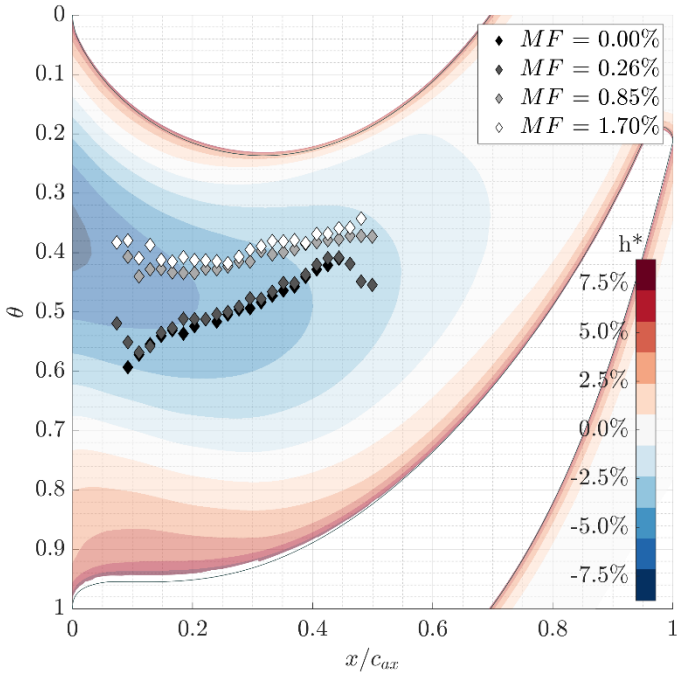

FIGURE 8: CASCADE VIEW OF VORTEX CORES AT A RANGE OF MF FOR THE EWC ROTOR. CONTOUR IS RADIAL HEIGHT OF EWC IN PERCENTAGE OF ANNULUS SPAN.

The alignment of the EV/PV to the trough continues through the measurement volume. The increase in purge flow causes a similar shift of the emergence position of the EV towards the SS. It should be noted that the difference in the initial position of the EV between the 0% and 1.7% *MF* cases is the same for the cylindrical and EWC rotor. However, the emergence of the EV is shifted approximately 5% of the blade pitch away from the SS at all flow rates from the cylindrical to the EWC rotor.

To emphasize the effect of purge flow rate and the presence of EWC on the system of vortices, Fig. 9 presents an axial slice at x/c_{ax} = 22% with isolines of $\gamma_2 = 0.5$, annotated with vortex core positions. For the 0% MF case, a single vortex system was observed at this level of γ_2 for both the cylindrical (Fig. 9a) and EWC (Fig. 9b) geometries, indicated here by the solid black and red isolines, respectively. The elongated (i.e. not circular) shape of the 0% MF isolines indicates the presence of two cores in the process of merging.

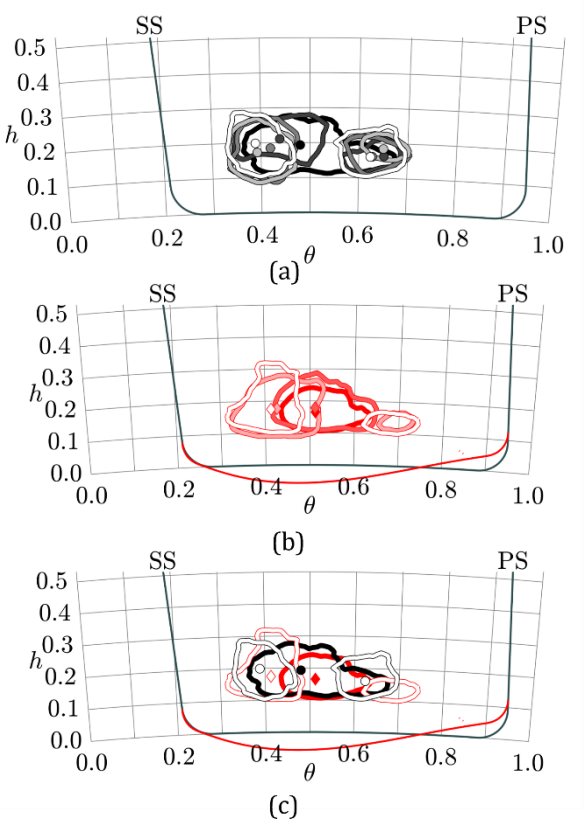

MF / Rotor	0.00%	0.26%	0.52%	0.85%	1.70%
Cyl.	●	●	●	●	○
EWC	♦	♦		♦	◇

FIGURE 9: ISOLINES OF γ_2 = 0.5 AT SINGLE AXIAL PLANE AT x/c_{ax} = 22%. (a) ALL *MFs* ON CYLINDRICAL ROTOR. (b) ALL *MFs* ON EWC ROTOR. (c) 0% & 1.7% *MFs* ONLY FOR BOTH ROTORS.

Fig. 9a shows the effect of purge flow rate on the vortex system present with the cylindrical rotor. The pitchwise shift of the EV with increasing MF is consistent with the conclusions resulting from Fig. 6; the radial migration of the EV with purge is consistent with Fig. 5. Fig. 9b concerns the EWC geometry: of note is the apparent dual vortex system for the two higher MFs, although no centroid was discernable for the PS-HSVs due to the low magnitude of γ_2. Fig. 9c directly compares the 0% and 1.7% MF cases for both rotor endwall geometries, which highlights the impact of the SS-trough on the secondary flow structure. The EV is closer to the endwall and circumferentially further from the SS, in accordance with the loci of the trough minima. The generally flattened shape of the isolines in Fig. 9c implies that the lower bound of the vortices may lie below the measurement interrogation volume.

4.3 Three-Dimensional Flow Field Analysis

While data so far has been presented in two-dimensional format, the volumetric PIV method offers three-component velocities that allow for representative flow field visualization and continuous vortex strength analysis. This subsection contains data for both the baseline and EWC rotors.

With three-dimensional velocity components available, it is possible to compare vortex-tracking parameters from the experimental data sets. Vortex parameters, like Q-criterion and vorticity, are not usually applicable to the experimental flow field data within a rotating turbine blade passage. Filtering the unstructured datasets allowed for experimentally obtained Q-criterion and non-dimensional vorticity fields with lower noise than the previously published data [3], though smoothing was required to be applied to the derivative-based parameters.

These two derivative-based methods and the aforementioned γ_2 method were applied to the measurement volume in Fig. 10. Isosurfaces of $\gamma_2 = 0.5$ were generated for each of the flow conditions and colored according to the radial position of the isocontour. To aid comparison, data are also displayed in stacked axial 2D planes within the blade passage in Fig. 10. The axial planes at ~10% c_{ax} intervals were arbitrarily chosen to show the change in field values throughout the data volume. Each row of Fig. 10 is a different experimental condition: 0% *MF* Cylindrical Rotor (Cyl.), 0% *MF* EWC, 1.7% *MF* Cyl. and 1.7% *MF* EWC, respectively. The rotor has been colored with a contour of surface altitude to distinguish the separate rotor configurations and highlight the relationship between the EWC and the position of the secondary flow structures. Each column of the figure is a separate vortex tracking parameter, γ_2 isosurfaces, and contours of γ_2, *Q-criterion* and ω^* respectively.

On any given row, it is clear that γ_2 is consistently tracking a system of vortices and is relatively devoid of noise. This parameter only indicates the presence of a vortex, whereas the others may be used to estimate its strength. Regions of positive Q and ω^* coincide with where γ_2 was able to identify vortical structures. The contours of the derivative functions show noisiness relative to γ_2 in all of the datasets. A similar magnitude of both Q and ω^* were obtained for all data, and the distribution of these parameters is similar when comparing the two rotors at the equivalent flow conditions.

For the cylindrical endwall (Fig. 10 a-d, i-l), the effect of purge on the secondary flow structures is apparent. The two initially distinct structures merge within the passage as the PS-HSV traverses from the PS towards the SS. The addition of purge changes the trajectory of the EV; due to the increase in radial momentum, the EV was further from the hub when it was first tracked (Fig. 10a & 10i) within the passage and continues on a radially outward path. The EV acts as a blockage, causing a delay in the cross-passage movement of the PS-HSV, which is consistently tracked on row 3 (Fig. 10i-l) of the figure.

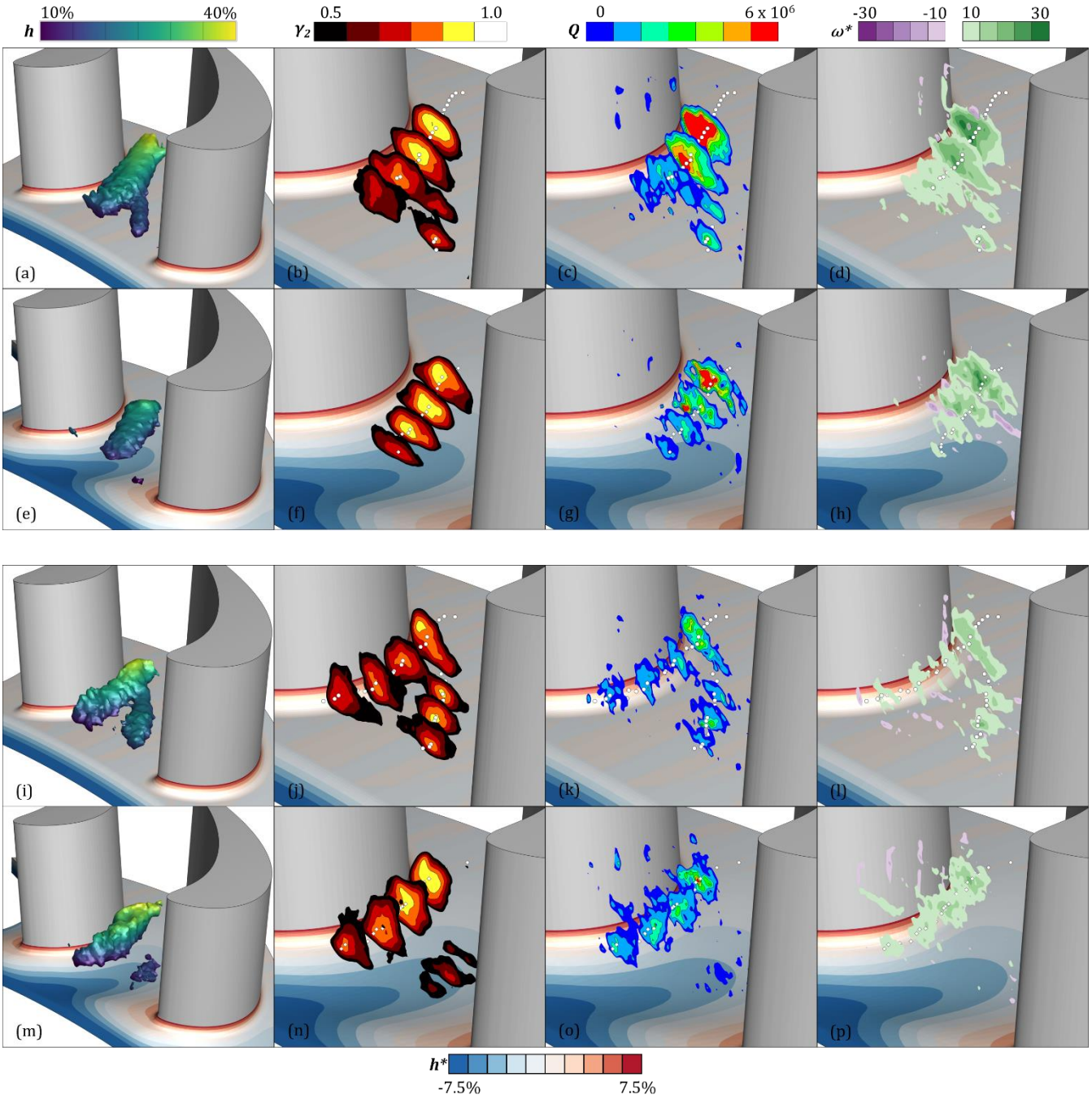

FIGURE 10: 3D VORTEX TRACKING. COLUMN 1 SHOWS $\gamma_2 = 0.5$ ISOSURFACE, COLOURED BY RADIAL HEIGHT. AXIAL PLANAR CONTOURS OF VORTEX-TRACKING PARAMETERS AT $x/c_{ax} = 10\%$, 20%, 30% AND 40%. COLUMN 2, γ_2; 3, Q-CRITERION; 4, NON-DIMENSIONAL VORTICITY, ω^*. ROW 1, 0% *MF* CYL.; 2, 0% *MF* EWC; 3, 1.7% *MF* CYL.; 4, 1.7% *MF* EWC. SYMBOLS REPRESENT VORTEX CORES.

With no purge (Fig. 10e-h), only one vortex was able to be tracked, and due to its location, it was inferred to be the EV. The vortex core was low in the passage, and closely followed the trough of the EWC. This is apparent in Fig. 10e, as the isosurface is a darker color

and is closer to the hub. The shape of the γ_2 contour in Fig. 10e and 10f suggest that the vortical structure extends below the measurement volume and is within 5% h of the hub. No second vortical structure is identified by any of the tracking parameters (Fig. 10g & 10h), either due to poor data quality around the LE feature of the EWC, or that no vortical structure exists. For the cylindrical rotor, early merging of the PS-HSV with the EV was seen; it is possible that the PS-HSV is encouraged to prematurely merge with the EV due to the EWC shape when the EV is relatively weak. Comparing the isosurfaces in Fig. 10a and 10e, the vortex structure is affected more by the EWC than the case with purge, as shown in Fig. 10i and 10m. The low momentum egress flow is strongly influenced by the combined rim-seal and EWC design.

At 1.7% MF, the EWC rotor (Fig. 10m-p) exhibited a similar flow field to the baseline rotor with consistent flow conditions (Fig. 10i-l). The EV emerged closer to the adjacent SS and migrated radially higher than the case with no purge, however the EWC was effective in limiting the extent of this shift with purge. Fig. 10m shows the vortical structure was initially closer to the EWC trough, as it guided the egress, which was introduced lower in the blade passage and with reduced radial momentum. Both γ_2 and Q show a low level of vortical activity downstream of the LE feature, suggesting a bifurcated secondary flow field for a rotor with 1.7% purge. Despite the initial low radius injection of the EV, the contour of radial height in Fig. 10m shows the final extent of the vortex in the aft passage was approaching that of the equivalent case on the Cyl. Rotor (Fig. 10i). Data obtained downstream of the stage would be required to assess this EWC and particular *MF*, given the vortices begin to converge upon a similar position in the blade passage.

The fourth column with contours of ω^* should be able to distinguish between clockwise and anticlockwise regions of rotation and was applied to CFD of this rotor in a previous study [23]. Past literature [2] was able to identify the SS-HSV orbiting around the PV, however, no significant regions of opposite rotation were seen relative to the dark green region associated with the EV in the Fig. 10d, h, l and p. The purple regions which are visible are primarily located at the edge of the dataset and are hence associated with errors in approximating the velocity derivative at the boundary.

4. CONCLUSION

This study presents a comparison of the secondary flow field in a turbine stage with and without rotor EWC. In the rotor without EWC, a monotonic shift in the emergence of the EV towards the SS is observed with an increase in purge flow rate. The use of an unstructured superposition of datasets allowed for more accurate velocity derivative approximations including the application of Q-criterion and a non-dimensional vorticity field, parameters typically reserved for numerical data. Regions of vortical structures identified by the γ_2 vortex identification parameter were corroborated with areas of high Q and vorticity.

This data, the first experimentally determined flow field within a rotating turbine stage with EWC to the authors' knowledge, directly shows the influence of EWC on the stage. Feature-based design practices of the EWC translated well from the CFD, due to the inclusion of purge flow in the simulations.

The rotor with non-axisymmetric EWC contained a LE feature near the PS and a trough closer to the SS. The EV was found to be affected by the features of the EWC as it was bound circumferentially and radially. The influence of the EWC on the secondary flow field was more apparent with no purge due to the low radial momentum of the egress fluid. A lack of vortical activity associated with the PS-HSV was noted in the rotor with EWC, consistent with the predictions.

ACKNOWLEDGEMENTS

The authors would like to thank Siemens Energy Industrial Turbomachinery Ltd. and the Engineering & Physical Sciences Research Council (EPSRC) for their financial support (grant EP/M026345/1). The experimental studies made use of the Versatile Fluid Measurement System enabled through EPSRC strategic equipment grant funding; EP/M000559/1 and EP/K040391/1. The authors thank Andrew Langley and Jim Cansell of the Department of Mechanical Engineering at the University of Bath for their expert technical support in this work.

APPENDIX: UNCERTAINTY ANALYSIS

An uncertainty analysis was conducted according to Mesny *et al.* [3], updated for the datasets presented here. The mean of the absolute components of velocity were u = 13.8 ms^{-1}, v = 6.1 ms^{-1} and w = 4.1 ms^{-1}. Components perpendicular to the focal plane were subject to displacement uncertainty of ±0.5 pixels, equivalent to ± 12 μm. Through-plane, Δz was scaled by particle triangulation to ± 2 pixels. The laser pulse Δt = 10μs was subject to the half-width-half-maximum uncertainty of ± 7 ns. The velocity magnitude uncertainty was therefore ± 1.1 ms^{-1} or ± 7.8%.

The unstructured processing allowed for enhanced understanding of the vector yield. Each flow condition comprised of a number of laser positions. For example, the MF = 0.26% EWC dataset contained 15 laser positions. The position of the laser within the passage led to a large variation in the number of vectors obtained from ~50k to ~600k. The total number of raw vectors obtained for this dataset was 3,494,305. The final number of vectors after spatial and statistical filtering is 227,605, representing a yield of 6.5%. This indicates

the difficulty in the acquisition of volumetric PIV data in a small region with a large number of reflections. The number of vectors within the measurement volume gave ~11 vectors/mm^3.

NOMENCLATURE

Acronyms

CCD	Charge Coupled Device
CFD	Computational Fluid Dynamics
EV	Egress Vortex
EWC	Endwall Contour[ing]
HSV	Horseshoe Vortex
LE	Leading Edge
MAD	Median-Average Deviation
MP	Mega Pixel
NGV	Nozzle Guide Vane
PIV	Particle Image Velocimetry
PS	Pressure-Side
PV	Passage Vortex
SS	Suction-Side
VV	Volumetric Velocimetry

Symbols

A	Integration Area (m^2)
b	Annulus Span (= 40 mm)
c_{ax}	Axial Chord (= 54 mm)
C_F	Flow Coefficient (= Re_x / Re_ϕ)
h	Dimensionless Spanwise Coordinate
h^*	EWC feature height (% of annulus span)
MF	Purge-Mainstream Mass Fraction

$\vec{n}$	Normal Vector
$\overrightarrow{PM}$	Radius Vector
Q	Q-Criterion
$\mathrm{Re_x}$	Axial Reynolds Number ($= \rho u r_s/\mu$)
$\mathrm{Re_\phi}$	Rotational Reynolds Number ($= \rho \Omega_\Phi {r_s}^2/\mu$)
r_s	Seal Radius (= 308 mm)
S	Symmetric Velocity Gradient Tensor
St	Stokes Number
u,v,w	Cartesian Velocities (m/s)
U_{in}	Average Axial Inlet Velocity (≈ 12.7 m/s)
$\vec{V}_{diff}$	Vector Difference (Filter)
$\overrightarrow{V_M}$	Velocity Vector (γ_2 calculation)
$\overrightarrow{V_P}$	Local Convection Velocity Vector
V_2	Bulk Relative Mainstream Velocity
Ω_Φ	Angular Velocity (= 30π rad/s)
x,y,z	Cartesian Coordinates (m)
Γ	Circulation (m^2s^{-1})
γ_2	Vortex Identification Parameter
$\eta_{mix,iso}$	Stage Efficiency (mix, iso definition)
Δt	Laser-pulse timestep (= 10 μs)
θ	Dimensionless Pitchwise Coordinate
ρ	Mainstream Density (kg/m^3)
ω	Vorticity (s^{-1})
ω^*	Non-dimensional Vorticity
Ω	Antisymmetric Velocity Gradient Tensor
Ω_Φ	Angular Velocity (rad/s)

REFERENCES

[1] Denton, J. D., 1993. "The 1993 IGTI Scholar Lecture: Loss Mechanisms in Turbomachines." *ASME J. Turbomach.*, 115(4): 621–656.
https://doi.org/10.1115/1.2929299

[2] Langston, L. S., 2001, "Secondary Flows in Axial Turbines—A Review," *Annals of the New York Academy of Sciences*, 934: 11-26.
https://doi.org/10.1111/j.1749-6632.2001.tb05839.x

[3] Mesny, A. W., Glozier, M. A., Pountney, O. J., Scobie, J. A., Li, Y. S., Cleaver, D. J., and Sangan, C. M., 2021. "Vortex Tracking of Purge-Mainstream Interactions in a Rotating Turbine Stage." *ASME J. Turbomach*, 144(4): 041011. https://doi.org/10.1115/1.4052690

[4] Rose, M. G., 1994. "Non-Axisymmetric Endwall Profiling in the HP NGV's of an Axial Flow Gas Turbine," Proceedings of the A 1994 International Gas Turbine & Aeroengine Congress & Exposition. Volume 1: Turbomachinery. The Hague, Netherlands. Jun 16, 1994. ASME Paper No. 94-GT-249, V001T01A090.
https://doi.org/10.1115/94-GT-249

[5] Hartland, J. C., Gregory-Smith, D. G., and Rose, M. G., 1998. "Non-Axisymmetric Endwall Profiling in a Turbine Rotor Blade." Proceedings of the ASME 1998 International Gas Turbine and Aeroengine Congress and Exhibition. Volume 1: Turbomachinery. Stockholm, Sweden. June 2–5, 1998. ASME Paper No. 98-GT-525, V001T01A130.
https://doi.org/10.1115/98-GT-525

[6] Harvey, N. W., Rose, M. G., Taylor, M. D., Shahpar, S., Hartland, J., and Gregory-Smith, D. G., 1999. "Nonaxisymmetric Turbine End Wall Design: Part I— Three-Dimensional Linear Design System." *ASME J. Turbomach.,* 122(2): 278–285.
https://doi.org/10.1115/1.555445

[7] Bergh, J., Snedden, G., and Reddy D., 2020. "Development of an automated non-axisymmetric endwall contour design system for the rotor of a 1-stage research turbine – part 1: System design." *Proc. Inst. Mech. Eng. A*, 234(5): 565-581.
https://doi.org/10.1177/0957650919876730

[8] Bergh J, Snedden G, and Reddy D., 2020. “Development of an automated non-axisymmetric endwall contour design system for the rotor of a 1-stage research turbine – Part 2 computed and experimental results”. *Proc. Inst. Mech. Eng. A*, 234(8): 1084-1100.
https://doi.org/10.1177/0957650919897769

[9] Bergh, J., & Snedden, G., and Dunn, D., 2020. “Optimization of Non-axisymmetric Endwall Contours for the Rotor of a Low Speed, 1 1/2 Stage Research Turbine with Unshrouded Blades - Optimization and Experimental Validation”. *ASME J. Turbomach.,* 142(4): 1-15.
https://doi.org/10.1115/1.4045988

[10] Jones, R. R., Pountney, O. J., Cleton, B. L., Wood, L. E., Deneys J. Schreiner, B., Carvalho Figueiredo, A. J., Scobie, J. A., Cleaver, D. J., Lock, G. D., and Sangan, C. M., 2019. "An Advanced Single-Stage Turbine Facility for Investigating Nonaxisymmetric Contoured Endwalls in the Presence of Purge Flow." *ASME J. Eng. Gas Turbines Power*, 141(12): 121008.
https://doi.org/10.1115/1.4045087

[11] Schneider, C. M., Schrack, D., Rose, M. G., Staudacher, S., Guendogdu, Y. and Engel, K., 2014. “On the interaction of streamwise vorticity with a rotating turbine blade,” 10th Eur. Conf. Turbomach. Fluid Dyn. Thermodyn., Lappeenranta, Finland. April 15-19, 2003. ETC Paper No. ETC2013-022, pp. 24–35.

[12] Schuepbach, P., Abhari, R. S., Rose, M. G., Germain, T., Raab, I., and Gier, J., 2010. “Effects of Suction and Injection Purge-Flow on the Secondary Flow Structures of a High-Work Turbine,” *ASME J. Turbomach.,* 132 (2): 021021.
https://doi.org/10.1115/1.4000485

[13] Regina, K., Kalfas, A. I., and Abhari, R. S., 2015. “Experimental Investigation of Purge Flow Effects on a High Pressure Turbine Stage,” *ASME J. Turbomach.,* 137 (4): 041006. https://doi.org/10.1115/1.4028432

[14] Schrewe, S., Werschnik, H., and Schiffer, H. P., 2013. “Experimental Analysis of the Interaction between Rim Seal and Main Annulus Flow in a Low Pressure Two Stage Axial Turbine,” *ASME J. Turbomach.,* 135(5), 051003. https://doi.org/10.1115/1.4023015

[15] Barsi, D., Lengani, D., Simoni, D., Venturino, G., Bertini, F., Giovannini, M., and Rubechini, F., 2022. "Analysis of the Loss Production Mechanism Due to Cavity–Main Flow Interaction in a Low-Pressure Turbine Stage." *ASME J. Turbomach.,* 144(9): 091004.
https://doi.org/10.1115/1.4053745

[16] Coull, J. D., and Clark, C. J., 2022. "The Effect of Inlet Conditions on Turbine Endwall Loss." *ASME J. Turbomach.,* 144(10): 101011.
https://doi.org/10.1115/1.4054443

[17] Chilla, M., Hodson, H. P., Pullan, G., and Newman, D. 2016. "High-Pressure Turbine Rim Seal Design for Increased Efficiency." Proceedings of the ASME Turbo Expo 2016: Turbomachinery Technical Conference and Exposition. Volume 2B: Turbomachinery. Seoul, South Korea. June 13–17, 2016. ASME Paper No. GT2016-57495, V02BT38A046.
https://doi.org/10.1115/GT2016-57495

[18] Schuepbach, P., Abhari, R. S., Rose, M. G., and Gier, J. 2011. "Influence of Rim Seal Purge Flow on the Performance of an Endwall-Profiled Axial Turbine." *ASME. J. Turbomach.,* 133(2): 021011.
https://doi.org/10.1115/1.4000578

[19] Regina, K., Kalfas, A .I., Abhari, R. S., Lohaus, A, Voelker, S, and auf dem Kampe, T., 2014 "Aerodynamic Robustness of End Wall Contouring Against Rim Seal Purge Flow." Proceedings of the ASME Turbo Expo 2014: Turbine Technical Conference and Exposition. Volume 2C: Turbomachinery. Düsseldorf, Germany. June 16–20, 2014. ASME Paper No. GT2014-26007, V02CT38A027.
https://doi.org/10.1115/GT2014-26007

[20] Hänni, D. D., Schädler, R., Abhari, R. S., Kalfas, A. I., Schmid, G., Lutum, E., and Lecoq, N., 2019. “Purge flow effects on rotor hub endwall heat transfer with extended endwall contouring into the disk cavity”. Journal of the Global Power and Propulsion Society, 3, 555-568. https://doi.org/10.33737/jgpps/109838

[21] Hu, S, and Luo, H., 2014. "Endwall Contouring Optimization in a High Pressure Turbine Vane With Consideration of Rim Seal Flow." Proceedings of the ASME Turbo Expo 2014: Turbine Technical Conference and Exposition. Volume 2C: Turbomachinery. Düsseldorf, Germany. June 16–20, 2014. ASME Paper No. GT2014-26587, V02CT38A039.
https://doi.org/10.1115/GT2014-26587

[22] Schäflein, L., Janssen, J., Brandies, H., Jeschke, P., and Behre, S., 2023. "Influence of Purge Flow Injection on the Performance of an Axial Turbine With Three-Dimensional Airfoils and Non-Axisymmetric Endwall Contouring." ASME. J. Turbomach., 145(6): 061004. https://doi.org/10.1115/1.4056238

[23] Schreiner, B. D. J., Wilson, M., Li, Y. S., and Sangan, C. M., 2019. "Design of Contoured Turbine Endwalls in the Presence of Purge Flow: A Feature-Based Approach." Proceedings of the ASME Turbo Expo 2019: Turbomachinery Technical Conference

and Exposition. Volume 2B: Turbomachinery. Phoenix, USA. June 17–21, 2019. ASME Paper No. GT2019-90443, V02BT40A007.

https://doi.org/10.1115/GT2019-90443

[24] Boomsma, A., and Troolin, D., 2018 "Time-Resolved Particle Image Identification and Reconstruction for Volumetric 4D-PTV" Proceedings of the 19th International Symposium on the Application of Laser Imaging Techniques to Fluid Mechanics. Lisbon, Portugal. July 16 – 19, 2018.

[25] Raffel, M., Willert, C. E., Scarano, F., Kähler, C. J, Wereley, S. T, and Kompenhans, J., 2018. *Particle Image Velocimetry : A Practical Guide.* 3rd Ed., Cham, Switzerland: Springer International.

https://doi.org/10.1007/978-3-319-68852-7

[26] Graftieaux, L., Michard, M., and Grosjean, N., 2001. "Combining PIV, POD and vortex identification algorithms for the study of unsteady turbulent swirling flows," Meas. Sci. and Technol., 12(9): 1422. https://doi.org/10.1088/0957-0233/12/9/307

[27] Hunt, J. C. R., Wray, A. A., and Moin, P., 1988. "Eddies, Streams and Convergence Zones in Turbulent Flows," Proceedings of the Summer Program in Centre for Turbulence Research. Paper No. N89-24555, pp. 193–208.

Table 1: Operating Parameters of the Turbine Stage.

Parameter	*Value*
Disc speed (rpm)	900
Rotational Reynolds Number, Re_ϕ	5.9×10^5
Axial Reynolds Number, Re_x	2.2×10^5
Flow Coefficient, C_F	0.38
Vane exit Mach Number, M	0.12
Degree of Reaction, Λ	0.21
Blade Loading Coefficient, Ψ	2.2
Blade Aspect Ratio (= b/c_{ax})	0.73
Blade Turning Angle (°)	104
Purge-Mainstream Mass Fraction, MF	0% - 1.7%

Figure 1: Endwall Contouring on a Turbine Blade Row. Arbitrary Contour Shows Positive and Negative Endwall Displacement.

Figure 2: University of Bath Optically Accessible Turbine [7].

Figure 3: Unsteady Fluctuation in Stage Efficiency Against Magnitude of Stage Efficiency for the Cylindrical and EWC Rotors, from [23]. Insets of Blade Sectors Colored by Surface Height as a Percentage of Span, h^*.

Figure 4: Turbine Cross Section with Laser Delivery; Modular Rotor Bling Highlighted.

Figure 5: In-plane Velocity Streamlines at Axial Planes x/c_{ax} = 10%, 20% and 30%, Contour of Normalized In-plane Velocity Magnitude. Each Row Represents a Purge-Mainstream *MF* from 0.0% to 1.7%. White Circles Represent Vortex Cores.

Figure 6: Cascade View of Vortex Cores at a Range of *MF* for the Cylindrical Endwall Rotor.

Figure 7: In-plane Velocity Streamlines at Axial Planes x/c_{ax} = 10%, 20% and 30% for the EWC Rotor, Contour of Normalized In-plane Velocity Magnitude. Each Row Represents a Purge-Mainstream *MF* from 0.0% to 1.7%. White Circles Represent Cylindrical Rotor Vortex Cores; Red Diamonds for the EWC. Red Line is EWC at each Axial Location.

Figure 8: Cascade View of Vortex Cores at a Range of MF for the EWC Rotor. Contour is Radial Height of EWC in Percentage of Annulus Span.

Figure 9: Isolines of γ_2 = 0.5 at Single Axial Plane AT x/c_{ax} = 22%. (a) All *MFs* on Cylindrical Rotor. (b) All *MFs* on EWC Rotor. (c) 0% & 1.7% *MFs* only for Both Rotors.

Figure 10: 3D Vortex Tracking. Column 1 shows γ_2 = 0.5 Isosurface, Coloured by Radial Height. Axial Planar Contours of Vortex-Tracking Parameters at x/c_{ax} = 10%, 20%, 30% and 40%. Column 2, γ_2; 3, Q-criterion; 4, Non-dimensional Vorticity, ω^*. Row 1, 0% *MF* CYL.; 2, 0% *MF* EWC; 3, 1.7% *MF* CYL.; 4, 1.7% *MF* EWC. Symbols Represent Vortex Cores.